J Mater Sci: Mater Electron
DOI 10.1007/s10854-013-1289-9

Influence of MoO_3 on electrical and microstructural properties of $(K_{0.44}Na_{0.52}Li_{0.04})(Nb_{0.86}Ta_{0.10}Sb_{0.04})O_3$

L. Ramajo · M. Castro · F. Rubio-Marcos · J. Fernandez-Lozano

Received: 23 February 2013 / Accepted: 7 May 2013

Abstract Microstructure, piezoelectric properties and dielectric behavior of undoped and MoO_3-doped lead-free $(K_{0.44}Na_{0.52}Li_{0.04})(Nb_{0.86-x}Ta_{0.10-x}Sb_{0.04-x})Mo_{5/6x}O_3$ were investigated. Samples were obtained by the conventional solid state reaction. X-ray diffraction (XRD) and Raman spectra revealed the formation of a perovskite phase, together with some minor secondary phase which could be assigned by XRD to $K_3LiNb_6O_{17}$. XRD also showed that the perovskite evolved from a tetragonal to orthorhombic symmetry with the increased doping level. The temperature dependence on real permittivity revealed the presence of a diffuse phase transition. This behavior raised with MoO_3 concentration. Also, dielectric relaxation processes were observed at room temperature resulting dependent on doping level and sintering time.

1 Introduction

Lead titanate–zirconate piezoceramics $PbZr_{(1-x)}Ti_xO_3$ (PZT) are the most important and widely used materials for piezoelectric transducers, transformers and sensors [1–3]. However the toxicity of lead is a serious threat to human health and the environment and thus lead-free piezoelectric ceramics have attracted great attention recently.

Numerous studies on lead-free piezoelectric ceramics such as $(K,Na)NbO_3$, $BaTiO_3$-based, Bi-layered, bismuth sodium titanate and tungsten bronze-type materials have been recently published [4–6]. In this way, niobates $(K,Na)NbO_3$ (KNN)-based ceramics have showed good piezoelectric and electric properties, high Curie temperature and environmental inequity. When the ratio of K/Na reaches 50/50, the piezoelectric coefficient reaches the highest point (up to 80 pC/N) [7]. This composition is reported to be composed of a virtual morphotropic phase boundary, where the total polarization can be maximized due to increased possibility of domain orientation. However, the exact crystallographic nature of this boundary in KNN is presently not well understood and it may be different than the one in lead-zirconate titanate solid solution [8].

On the other hand, Saito et al. [9] reported exceptionally high piezoelectric properties in the system $(K,Na)NbO_3$–$LiTaO_3$–$LiSbO_3$. This study was based on chemical modifications, in the vicinity of the MPB of $(K,Na)NbO_3$ (KNN), by complex simultaneous substitutions in the A (Li) and B (Ta and Sb) site of the perovskite lattice. In this way, similar composition with 4 mol % of Lithium and 10 mol % of tantalum substituted KNN ceramic prepared by simple pressureless solid state sintering without aid additives or special powder handling reach interesting properties with $d_{33} < 160$ pC/N without antimony [10].

In this paper, undoped and MoO_3-doped lead-free $(K_{0.44}Na_{0.52}Li_{0.04})(Nb_{0.86-x}Ta_{0.1-x}Sb_{0.04-x})Mo_{5/6x}O_3$ (KNL–NTS), were prepared by a solid state reaction. Experimental results were discussed considering the MoO_3 effect on structure, microstructure, dielectric and piezoelectric properties of KNL–NTS-based ceramics.

2 Experimental

The $(K_{0.38}Na_{0.52}Li_{0.04})(Nb_{0.86-x}Ta_{0.10-x}Sb_{0.04-x})Mo_{5/6x}O_3$ composition was prepared by the conventional ceramic

L. Ramajo (✉) · M. Castro
Instituto de Investigaciones en Ciencia y Tecnología de Materiales (INTEMA), Juan B Justo 4302, B7608FDQ Mar del Plata, Argentina
e-mail: lramajo@fi.mdp.edu.ar

F. Rubio-Marcos · J. Fernandez-Lozano
Instituto de Cerámica y Vidrio de Madrid (ICV), Campus UAM c/Kelsen 5, Madrid, Spain

Published online: 26 May 2013

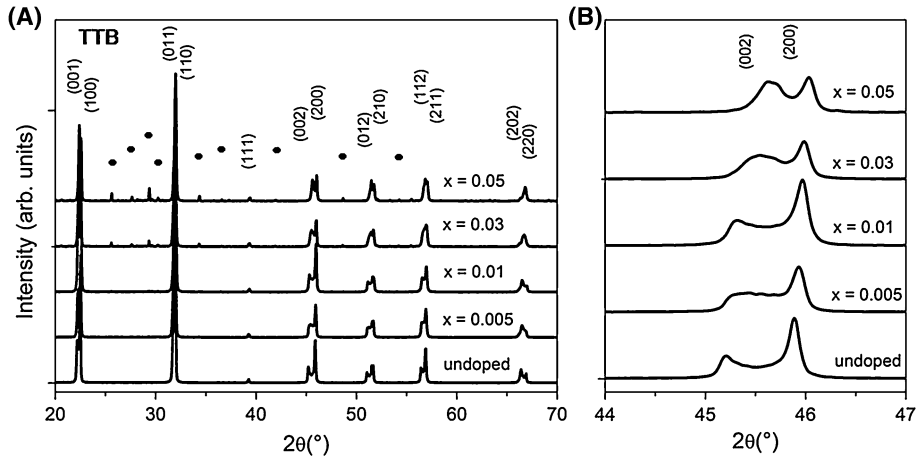

Fig. 1 XRD patterns corresponding to the KNL–$(NTS)_{1-x}Mo_{5x/6}$ ceramics sintered at 1,125 °C for 2 h (**a**). The inset shows magnified patterns in the 44–47° 2θ range (**b**)

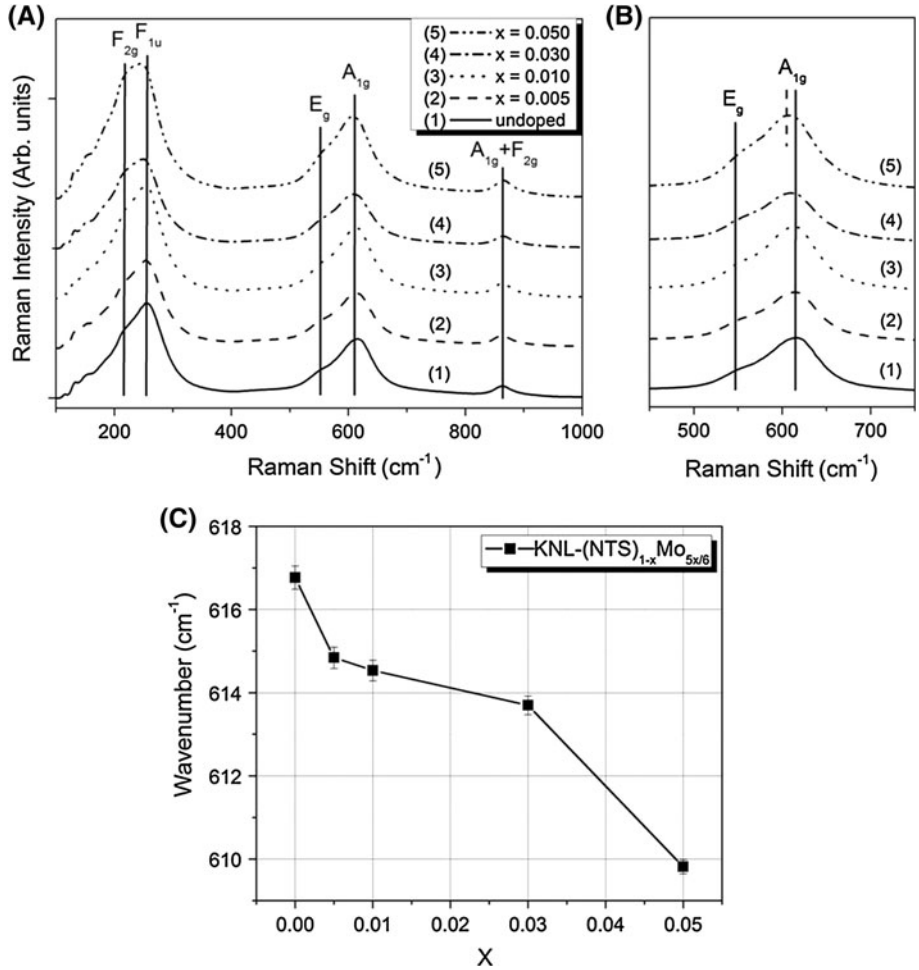

Fig. 2 Raman spectra KNL–$(NTS)_{1-x}Mo_{5x/6}$ ceramics sintered at 1,125 °C for 2 h in the range of the Raman shift from 100 to 1,000 cm^{-1} (**a**). The inset shows magnified patterns in the 450–750 cm^{-1} range (**b**). υ_1 Raman modes values obtained by fitting the experimental data as a function of Mo concentration (**c**)

processing route. Na_2CO_3, Li_2CO_3 (Panreac, 99.5 %), K_2CO_3 (Merck, 99 %), MoO_3, Nb_2O_5, Ta_2O_5, and Sb_2O_5 (Sigma–Aldrich, ≥99.5, 99.9, 99 and 99.995 %, respectively) were used as starting raw materials. They were individually milled, in order to obtain an appropriate distribution of the particle size.

Powders with different MoO_3 concentrations (x = 0, 0.005, 0.010, 0.030 and 0.050 mol %), abbreviated as KNL–$(NTS)_{1-x}Mo_{5x/6}$, were mixed and milled in ethanol medium in a high energy laboratory ball-mill with zirconia balls for 3 h. Afterwards, the resulting powders were dried and calcined at 700 °C for 2 h at 3 °C/min. The calcined powders

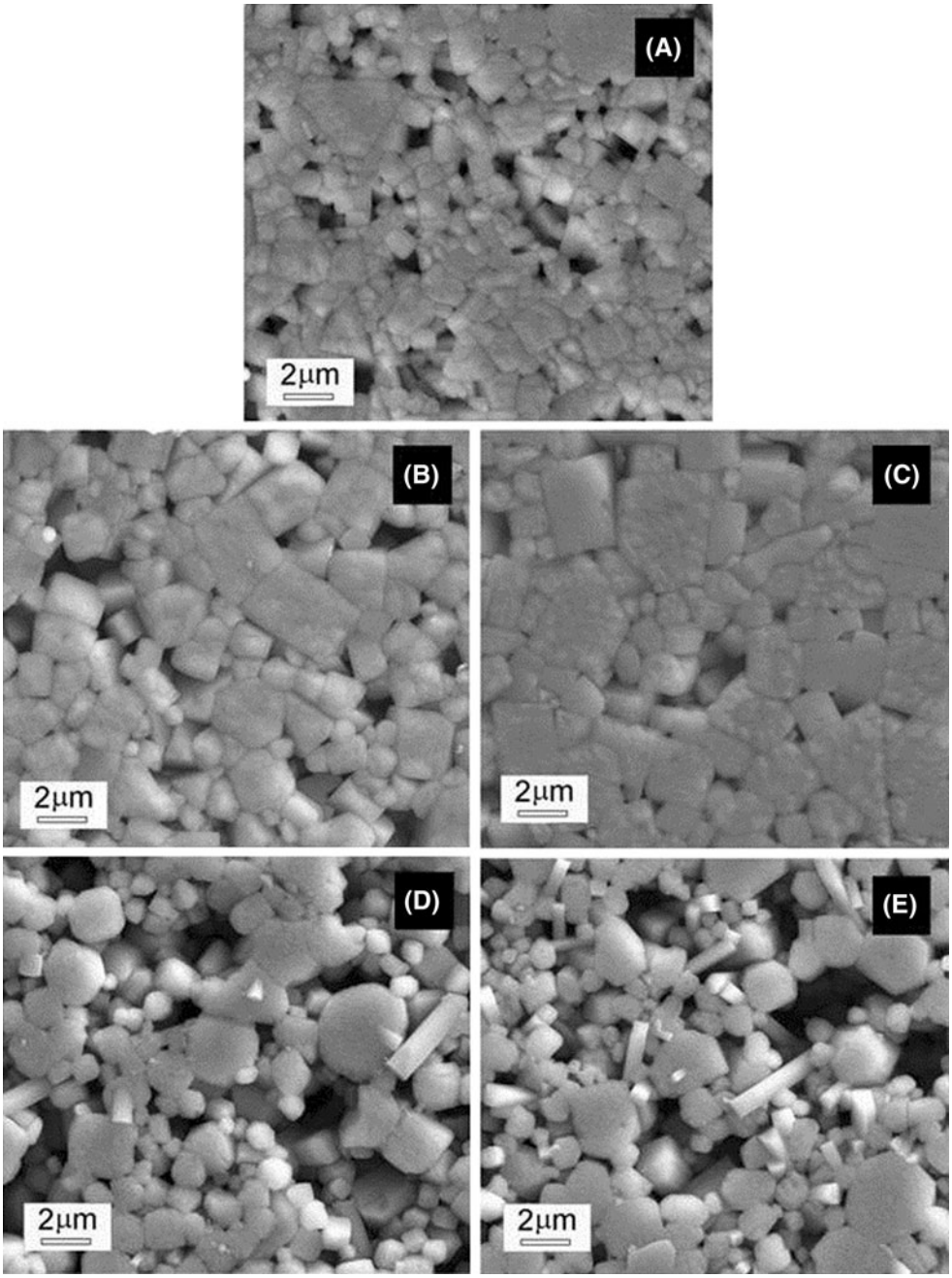

Fig. 3 SEM images of KNL–$(NTS)_{1-x}Mo_{5x/6}$. **a** undoped; **b** x = 0.005 **c** x = 0.010; and **d** x = 0.030 and **e** x = 0.050

Table 1 Density (ρ), average particle size (D_{50}), dielectric properties (ε_r, tan δ at 2,500 Hz), and piezoelectric constant (d_{33}) of KNL–$(NTS)_{1-x}Mo_{5x/6}$ sintered ceramics

KNL–$(NTS)_{1-x}Mo_{5x/6}$ (mol %)	ρ (g/cm^3)	D_{50} (μm)	ε_r	tan(δ)	d_{33} (pC/m)
0.000	4.41 ± 0.02	1.32 ± 0.50	880	0.008	230
0.005	4.43 ± 0.03	1.60 ± 0.62	690	0.036	200
0.010	4.47 ± 0.07	1.87 ± 0.80	660	0.062	185
0.030	4.05 ± 0.02	1.25 ± 0.62	454	0.090	162
0.050	3.99 ± 0.02	1.26 ± 0.62	390	0.101	95

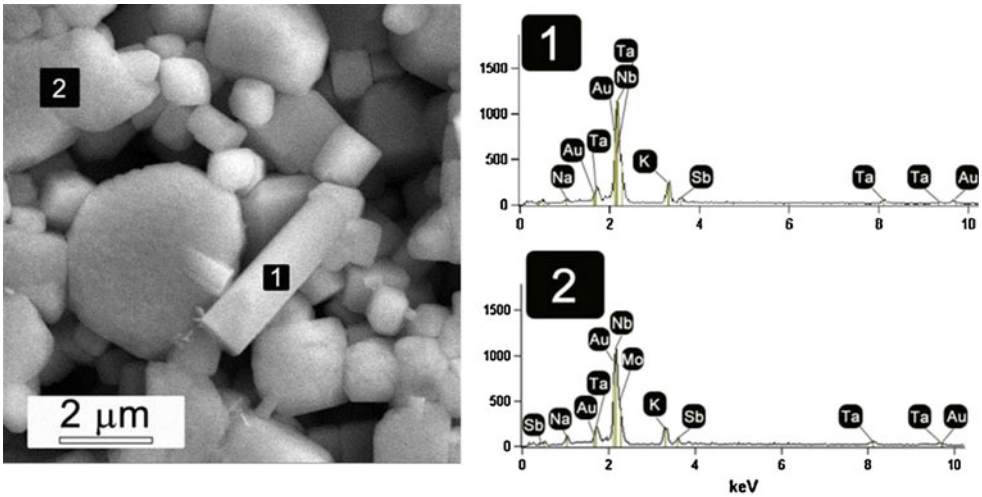

	O	Na	K	Nb	Mo	Sb	Ta
1	62.67	5.41	9.28	19.61	0.00	1.29	1.74
2	61.21	9.95	7.35	18.27	0.27	0.92	2.03

Fig. 4 Energy dispersive spectra (EDS) at two different regions (1 and 2) of KNL–$(NTS)_{1-x}Mo_{5x/6}$ with x = 0.030. The table shows the composition on the points shown on Figure derived from EDS spectra. The table represents the atomic percentages of elements

were attrition milled again and pressed at 200 MPa into disks of 10 mm in diameter and 0.7 mm thick. The pellets were finally sintered in air at 1,125 °C for 2 h.

Crystalline phases were characterized by X-ray diffraction (XRD) (D8 Advance, Bruker, Germany), using CuKα radiation, on powders obtained by milling the sintered ceramics. The Raman scattering was measured in air atmosphere and at room temperature. The experiments were performed using a Confocal Raman microscope coupled to an AFM (Witec alpha-300R). Raman spectra were obtained using a 532 nm excitation laser and a 100× objective lens (NA = 0.9). The incident laser power was 0.5 mW. The optical diffraction resolution of the Confocal Microscope was limited to about ~200 nm laterally and ~500 nm vertically. Raman spectral resolution of the system was down to 0.02 cm^{-1}. Samples were deposited on a microscopy glass slide and mounted on a piezo-driven scan platform having 4 nm lateral and 0.5 nm vertical positioning accuracy. Collected spectra were analyzed by using Witec Control Plus Software.

Microstructure was evaluated on polished and thermally etched samples (1,000 °C for 5 min) using a field emission scanning electron microscope, FE-SEM (Hitachi S-4700). For the electrical measurements, a fired silver paste was used for the electric contacts. The samples were poled in a silicon oil bath at 25 °C by applying a DC field of 4.0 kV/mm^{-1} for 30 min.

The piezoelectric constant d_{33} was measured using a piezo d_{33} meter (YE2730A d_{33} METER, APC International, Ltd., USA). Dielectric properties were determined at different temperature and frequencies using an impedance analyzer HP4294A in the frequency range 100 Hz–1 MHz. Finally, the ferroelectric nature of the ceramics was determined using a hysteresis meter (RT 6000 HVS, RADIANT Technologies).

3 Results and discussion

Figure 1 displays the XRD patterns of the KNL–$(NTS)_{1-x}Mo_{5x/6}$ ceramics for different MoO_3 amounts and sintered at 1,125 °C for 2 h. Diffraction peaks could be indexed to a perovskite with tetragonal structure [11]. Also peaks corresponding to a minor secondary phase assigned to $K_3LiNb_6O_{17}$ (PDF#36-0533) with tetragonal tungsten–bronze structure TTB [7], are detected. Moreover, the addition of MoO_3 induces a phase diffusion transition between a tetragonal phase and a weak orthorhombic phase (Fig. 1b) and increases the secondary phase amount (Fig. 1a). Therefore, these results indicate that the TTB phase formation is strongly influenced by the MoO_3 content. On the other hand, the coexistence of different polymorphs (tetragonal and orthorhombic) was also reported for this composition [7].

The Raman spectra of the KNL–$(NTS)_{1-x}Mo_{5x/6}$ samples sintered for 2 h are shown in Fig. 2. In all samples, the main vibrations are associated to the BO_6^- perovskite octahedron [12]. So, the vibrations of the BO_6^- octahedron consist of $1A_{1g}$ (υ_1) + $1E_g$ (υ_2) + $2F_{1u}$ (υ_3, υ_4) + F_{2g} (υ_5) + F_{2u} (υ_6). From these vibrations, $1A_{1g}$ (υ_1) + 1Eg (υ_2) + $1F_{1u}$ (υ_3) are stretching modes and the other ones bending modes. In particular, A_{1g} (υ_1) and F_{2g} (υ_5) have been detected as being relatively strong scatterings in systems similar to the one studied in this paper due to a near-perfect equilateral

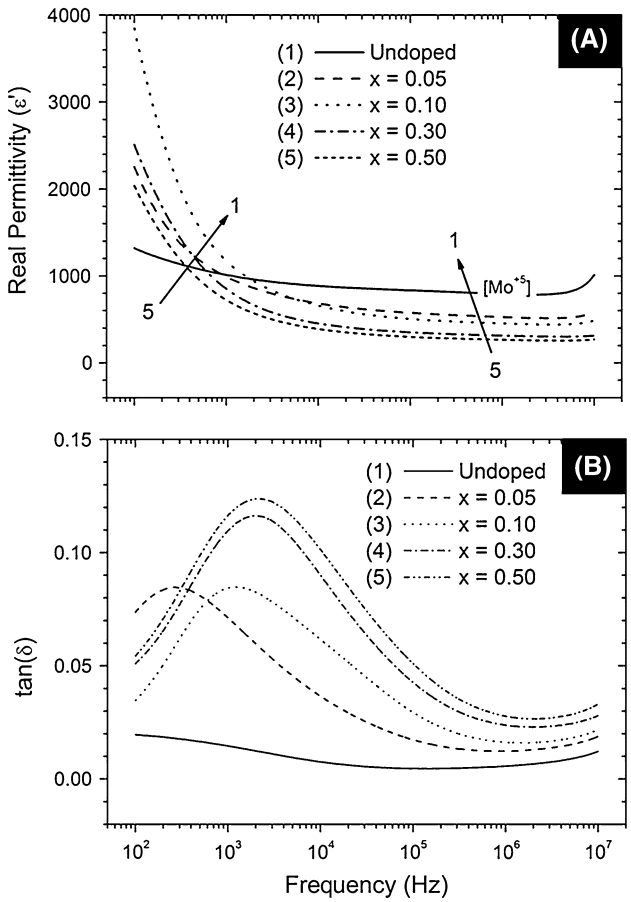

Fig. 5 Real permittivity **(a)** and loss tangent **(b)** as a function of frequency and doping level of the KNL–$(NTS)_{1-x}Mo_{5x/6}$ ceramics

octahedral symmetry. Changes in the Raman shift of modes associated to the BO_6^- octahedron allow determining variations in polarization, which are associated with modifications of the constant force of the octahedron due to deformation or stress. In this way, Fig. 2c shows the A_{1g} (υ_1) mode evolution with MoO_3 concentration that were fitted using a sum of Lorenzian functions.

The incorporation of Mo^{6+} into the perovskite lattice slightly alters the observed vibrations frequencies as shown in Fig. 2. The peak A_{1g} (υ_1) shifts to lower wavenumber as MoO_3 content increases, see Fig. 2b and c, due to a decrease in the strength constant force, caused by the lengthening of the distance between B^{5+} type ions and their coordinated oxygens. As we noticed in a previous study [9], the evolution of the A_{1g} (υ_1) Raman shift is similar to the evolution observed by XRD (see Figs. 1b and 2b): for low MoO_3 content, there is a slight evolution of the Raman shift, while for $x > 0.03$, the Raman bands are substantially redshifted.

The microstructural evolution of KNL–NTS ceramics as a function of MoO_3 concentration is shown in Fig. 3. The FE-SEM micrographs show the KNL–$(NTS)_{1-x}Mo_{5x/6}$ morphology consisting of faceted grains and cube-shaped grains. Undoped sample shows a porous microstructure containing small grains without secondary phases. On the other hand, low doped specimens present large grains with low porosity level (see Table 1). A change in the average grain size and the grain morphology is observed with the MoO_3 content, as depicted in Fig. 3d, e. In addition, for higher MoO_3 content ($x \geq 0.03$) secondary re-crystallization begins to appear and its morphology consists on small plate-like grains see Fig. 3d, e. According to XRD results, secondary phases are observed and their amount increased with the doping level.

EDS analysis was carried out on the specimens with $x = 0.030$ to identify the composition of the TTB phase. Figure 4a, b illustrate the EDS spectra corresponding to the matrix and TTB phase, respectively, and the composition analysis is also summarized in the included table. Na, K, Nb, Sb, Mo and Ta ions were found in the matrix and its composition was confirmed to be the very close to KNL–$(NTS)_{0,95}Mo_{0,042}$, see composition table of the Fig. 4 derived from EDS spectra. In the TTB phase, however, a high concentration of K and Sb ions has been detected without the presence of Mo ions, see composition table of the Fig. 4. Therefore, the TTB phase was considered to be Na and Mo deficient due to the Na_2O evaporation, and the poor recrystallization of TTB phase with the MoO_3 presence.

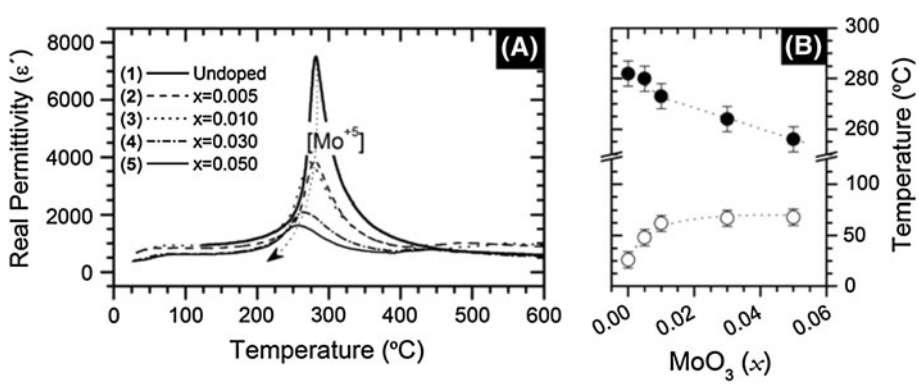

Fig. 6 Real permittivity (ε′) as a function of temperature of KNL–$(NTS)_{1-x}Mo_{5x/6}$ sintered ceramics (at 50 kHz) (**a**). Curie temperature (Tc) (*filled circle*) and orthorhombic-tetragonal transition phase (*empty circle*) as a function of MoO_3 amount (**b**)

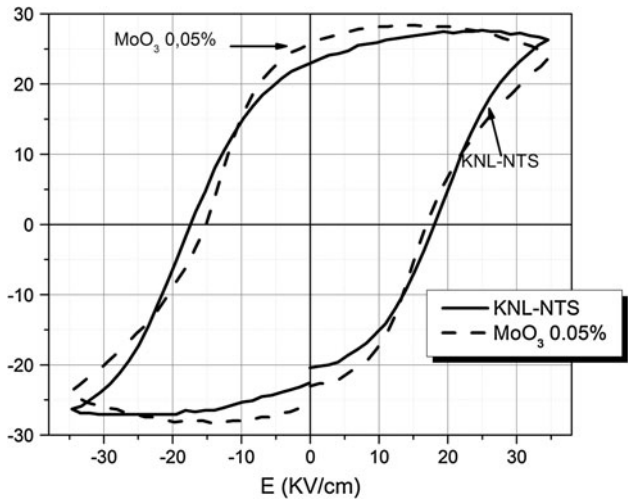

Fig. 7 Hysteresis loops at room temperature of KNL–$(NTS)_{1-x}Mo_{5x/6}$ sintered ceramics

Table 1 shows density, real part (ε′) of dielectric constant, dielectric loss (tanδ) and piezoelectric constant of sintered samples. It can be observed that, ceramics doped with 0.010 mol % show higher density values than pure KNL–NTS ceramics, although a diminution in ε_{33} and d_{33} values has been observed when the doping level increases. This behaviour can be attributed to the secondary phase formation and the coexistence of different polymorphic phases.

Mo-doping also modified dielectric response. In this way, Fig. 5a, b show real part (ε′) of dielectric permittivity, and dielectric loss (tanδ) of the KNL–$(NTS)_{1-x}Mo_{5x/6}$ ceramics at different frequencies. At high frequency, dielectric permittivity decreases with the doping level. Undoped ceramic presents a stable value within this frequency range while doped samples show a relaxation process. Also, the corresponding peak in the dielectric loss is observed in doped samples. This behavior, in the whole frequency range, could be associated with the increased porosity level, the amount of secondary phases, and the orthorhombic symmetry stabilization with the addition MoO_3.

The high density KNL–$(NTS)_{1-x}Mo_{5x/6}$ ceramics are perfectly adapted to measure the dielectric, ferroelectric and piezoelectric properties, and to try to correlate such properties to the observed structural evolution with MoO_3 addition. Figure 6a, b show the temperature dependence of the real permittivity ε′ (at 50 kHz) of KNL–$(NTS)_{1-x}Mo_{5x/6}$ ceramics as a function of x. These curves present two transitions with temperature. The first one, near room temperature, is associated to the orthorhombic-tetragonal phase transition (To–t), while the second one, at 280 ± 5 °C, corresponds to the ferroelectric–paraelectric phase transition (Curie temperature, *Tc*). In this way, Tc slightly moves toward low temperatures with the MoO_3-doping concentration.

The real permittivity peaks at T_C are sharp and the highest values correspond to the pure KNL–NTS. On the other hand, the temperature of the orthorhombic-tetragonal phase transition (*T*o–t) is increased by MoO_3 addition (Fig. 6) which corresponds well with the XRD observation. Such increase in the *T*o–t value suggests that the Mo^{6+} incorporation stabilizes the orthorhombic symmetry at room temperature. This phenomenon has been found in other compounds such as (Pb, La)(Zr, Ti)O_3 and doped $BaTiO_3$ [13–15]. It is suggested that a transition from a normal ferroelectric to a 'relaxor-like' ferroelectric is due to the cation disorder in the perovskite unit cell and the consequent micro domain formation [16].

Finally, specimens with the lowest porosity are analyzed under an external strong electric field, exhibiting in all cases ferroelectric behavior due to spontaneous polarization. Hysteresis loops of pure and 0.005 mol % doped-KNL–NTS, at room temperature under an a.c. electric field of $E_p = 35$ kV/cm are shown in Fig. 7. Undoped ceramics show a remnant polarization (P_r) of ~20 μC/cm^2, slightly lower than the value measured in the doped sample (~23 μC/cm^2). Also, the coercive field values, *E*c, of doped-ceramics are similar to pure KNL–NTS. Higher saturation values (P_s) are 24.9 and 25.8 for pure and doped KNL–NTS. The similarity values between pure and doped ceramic could be attributed to comparable grain size, microstructure, dielectric permittivity and density values.

4 Conclusions

The effect of MoO_3 on the microstructure, phase transition and electric properties of KNL–$(NTS)_{1-x}Mo_{5x/6}$ systems obtained by the conventional mixed oxide method has been reported. X-ray diffraction patterns showed the formation of a solid solution of Mo^{6+} in KNL–NTS with perovskite-type structure. In this case, two different symmetries were presented (tetragonal and orthorhombic), together with the presence of a TTB phase. In this way, the TTB amount increases with the doping level.

The grain size, microstructure morphology, transition temperatures and real permittivity were modified with the doping concentration. Samples with low additive concentration exhibited high density values and dielectric constant. In opposition, samples with the highest MoO_3 addition exhibit low density values and high dielectric losses.

Doped KNL–NTS presented a relaxation process at room temperature associated with relaxor behavior, which is related to a transition orthorhombic–tetragonal polymorphic phase transition (*T*o–t).

The temperature dependence of real permittivity showed a phase transition, related to tetragonal-cubic character and this character was more obvious with increasing concentration of Mo.

Acknowledgments The authors are grateful to CONICET, ANCPyT (Argentina) and MICINN project MAT 2010-21088-C03-01 for the financial support provided for this research. Dr. F. Rubio-Marcos is also indebted to CSIC for a "Junta de Ampliación de Estudios" contract (ref. JAEDOC071).

References

1. Z.P. Yang, Y.F. Chang, H. Li, Mater. Res. Bull. **40**, 2110–2119 (2005)
2. H. Du, S. Qu, J. Che, Z. Liu, X. Wei, Z. Pei, Mater. Sci. Eng. A **393**, 36–41 (2005)
3. X. Zhai, H. Wang, J.-W. Xu, C.-L. Yuan, X.-W. Zhang, C.-R. Zhou, X.-Y. Liu, J. Mater. Sci. Mater. Electron. **24**, 687–691 (2013)
4. X. Pang, J. Qiu, K. Zhu, J. Luo, J. Mater. Sci. **46**, 2345–2349 (2011)
5. A. Thongtha, T. Bongkarn, Eng. Mater. **474**, 1754–1759 (2011)
6. H. Wang, R. Zuo, Y. Liu, J. Fu, J. Mater. Sci. **45**, 3677–3682 (2010)
7. L. Ramajo, R. Parra, M.A. Ramírez, M.S. Castro, Bull. Mater. Sci. **34**, 1213–1217 (2011)
8. Hansu. Birol, Dragan. Damjanovic, Nava. Setter, J. Eur. Ceram. Soc. **26**, 861–866 (2006)
9. Y. Saito, H. Takao, T. Tani, T. Nonoyama, K. Takatori, T. Homma, T. Nagaya, M. Nakamura, Nature **432**, 84–87 (2004)
10. F. Rubio-Marcos, J.J. Romero, M.S. Martín-Gonzalez, J.F. Fernández, J. Eur. Ceram. Soc. **30**, 2763–2771 (2010)
11. F. Rubio-Marcos, P. Ochoa, J.F. Fernández, J. Eur, Ceram. Soc. **27**, 4125–4129 (2007)
12. F. Rubio-Marcos, P. Marchet, T. Merle-Méjean, J.F. Fernandez, Mater. Chem. Phys. **123**, 91–97 (2010)
13. N.A. Hegab, A.E. Bekheet, M.A. Afifi, L.A. Wahaba, H.A. Shehata, J. Ovonic, Research **3**, 71–82 (2007)
14. Y. Guo, K. Kakimoto, H. Ohsato, Solid State Commun. **129**, 279–284 (2004)
15. M. Kosec, V. Bobnar, M. Hrovat, J. Bernard, B. Malic, J. Holc, J. Mater. Res. **19**, 1849–1854 (2004)
16. Y. Chang, Z. Yang, L. Wei, B. Liu, Mater. Sci. Eng. A **437**, 301–305 (2006)